Construction and Building Materials 526 (2026) 146424

Contents lists available at ScienceDirect

Construction and Building Materials

journal homepage: www.elsevier.com/locate/conbuildmat

Fire resistance of fly ash–ladle slag based geopolymer: Insights on recrystallization of waste glass at high temperature

Jiale Yuan [a], Xuan Ling [a], Yanjie Tang [b], Yan Luo [a], Yanshuo Liu [a], H.J.H. Brouwers [a], Qingliang Yu [a,*]

[a] Department of the Built Environment, Eindhoven University of Technology, P.O. Box 513, Eindhoven 5600MB, the Netherlands
[b] Department of Civil and Environmental Engineering, The Hong Kong Polytechnic University, Kowloon, Hong Kong, China

ARTICLE INFO

Keywords:
Ternary geopolymer
Fire resistance
Waste glass
Elevated temperature
Phase recrystallization
Microstructure evolution

ABSTRACT

Improving the fire resistance of alkali-activated blend systems remains a challenge. This study investigates the use of waste glass (WG) to strengthen the high–temperature performance of a class F fly ash (FA)–ladle slag (LS) hybrid system through its recrystallization at elevated temperatures. The results indicate that the moderate incorporation of WG enhances the fire resistance of the pastes. The sample containing 20% WG exhibits the highest strength retention ratio at 800 °C, reaching 2.57 times that at ambient temperature. As temperature rises, the incorporation of WG promotes the formation of Ca-enriched gel products by releasing additional Ca and facilitates the development of crystalline phases through the recrystallization of gel products and unreacted WG, thus enhancing the residual strength. Meanwhile, elevated temperatures accelerate crack propagation and pore coarsening, whereas microcracks and micropores are healed by the melted unreacted WG and viscous sintering of geopolymer. Overall, this study provides in-depth insights into the strength evolution mechanism induced by WG at elevated temperatures, contributing to the potential application of WG for fire resistant geopolymer.

1. Introduction

Fire is a frequent and destructive hazard worldwide, posing a significant threat to public safety and structural service life. When subjected to elevated temperatures, Ordinary Portland Cement (OPC) exhibits limited fire-resistant ability due to the dehydration and decomposition of hydration products, leading to mechanical degradation and structural collapse [1]. As an attractive alternative to OPC materials, geopolymer synthesized from aluminosilicate precursors such as Class F fly ash (FA) and metakaolin (MK) exhibits superior fire resistance due to the better thermally stable aluminosilicate gel structure [2,3]. However, the pure geopolymer systems, especially those based on low calcium FA, always exhibit lower early strength, which limits their engineering applications. To address this limitation, alkali-activated fly ash–slag (AAFS) systems have been developed by incorporating additional calcium sources such as ground granulated blast furnace slag (GGBS) to accelerate reaction kinetics and improve early strength [4–6]. Nevertheless, the C–A–S–H gel and N–A–S–H gel exhibit incompatibility in thermal response within an AAFS system. C–A–S–H is easier to thermally decompose than N–A–S–H, leading to strength degradation compared to alkali-activated fly ash (AAF) systems [7].

To date, extensive efforts have been devoted to enhancing the fire resistance of AAFS-based systems. However, approaches relying on adjusting the proportions of conventional precursors and different activators to regulate gel compatibility exhibit limited effectiveness, as the modified systems still suffer strength loss at high temperatures due to the presence of C–A–S–H gel [4,8,9]. In addition, many studies aim to improve the microstructure characteristics to enhance fire resistance, such as incorporating fibers to suppress cracks propagation and adding chemical admixtures to refine the pore structure [10–14]. For instance, Yu et al. [13] found that the incorporation of steel fibers improved residual compressive strength retention of geopolymer mortar and concrete, whereas all samples exhibited strength degradation as the temperature increased. A similar trend was observed in the study by Chan and Zhang [14], which employed PVA fibers. Beyond the fiber-reinforced systems, applying other microstructural modifications, such as foamed systems, strength loss at high temperatures has still been observed [10]. Although these strategies are feasible in mitigating strength loss, they fail to enhance residual strength relative to those at

* Corresponding author.
E-mail address: q.yu@bwk.tue.nl (Q. Yu).

https://doi.org/10.1016/j.conbuildmat.2026.146424
Received 3 January 2026; Received in revised form 15 April 2026; Accepted 18 April 2026

room temperature. Further, many of these methods are not economically favorable for practical applications. In terms of phase composition, Al-rich precursors are beneficial for improving high temperature performance because they promote the formation of thermally stable gel frameworks and crystals. Our previous studies indicate that ladle slag (LS), which contains a higher Al content than GGBS, provides better fire-resistance performance when incorporated into FA-based geopolymers [7,15]. Fundamentally, the further enhancement of high-temperature resistance is governed by microstructural optimization and more fire-resistant phases formation. Therefore, innovative and cost-effective solutions targeting physical and chemical improvements at high temperatures are required.

As a common solid waste, waste glass (WG) shows great potential for high-temperature resistant applications owing to its melting and crystallization behavior under elevated temperatures, which can refine pore structure and generate thermally stable supplementary crystals such as wollastonite whose melting point is 1540 °C [16]. The incorporation of WG in alkali-activated material (AAM) systems has emerged as a promising pathway for its valorization. However, current studies predominantly focus on the application of WG under ambient conditions, while the systematic investigations into the influence of WG as a precursor on the high-temperature performance of AAMs remain relatively limited. Lu and Poon [17] found both replacing either FA or GGBS with WG improved the residual compressive strength of alkali-activated mortar at 800 °C. Similarly, Derinpinar et al. [18] observed that the increased substitution of WG with GGBS led to decreased compressive strength at room temperature but improved the high temperature resistance of geopolymer concrete. Jiang et al. [19] identified that the incorporation of WG enhanced the fire resistance in FA-based geopolymer pastes, and observed that the melted WG filled the porous structures of matrix, thus refining the pore system. These findings suggest that WG incorporation can mitigate strength loss at elevated temperatures. The potential melting of WG can improve the pore structure by healing internal pores and cracks, thereby enhancing fire resistance. Nevertheless, existing studies mainly focused on the mitigation of strength degradation through molten-glass healing, while the WG dosage-dependent strengthening/deterioration threshold and its coupled effects on crystallization phase transformation and pore evolution in AAM systems remain insufficiently clarified.

At high temperatures, another notable feature of WG is that it can act as a fluxing agent in combination with other solid wastes for ceramic production [20–23]. Huang et al. [20] produced glass-ceramics using WG and incinerated sewage sludge ash and found that the increased WG content densified the microstructure and promoted the formation of crystalline phases. Similar results were reported by Zeng et al. [22], who used WG and coal fly ash for glass-ceramics. Additionally, WG inherently undergoes partial crystallization when exposed to high temperatures. Lin et al. [24] observed that the crystallization degree of WG increased as the temperature rose from 600 °C to 850 °C, with the main crystalline phases being calcium aluminum oxide, cristobalite, and wollastonite. Yao et al. [25] identified that the devitrite was initially formed and then transformed into wollastonite with the temperature increasing from 950 °C to 1200 °C. In summary, the utilization of WG promotes the increased formation of crystalline phases that play a crucial role in improving the thermal stability of AAMs. Therefore, the effect of WG as a precursor on the formation and evolution of crystalline phases merits further exploration.

Herein, this study aims to incorporate WG into the FA and LS hybrid system and provide a comprehensive understanding of the role of WG in enhancing the high temperature performance within a ternary geopolymer system at different temperatures (20 °C, 400 °C, 600 °C, 800 °C). The influence of WG on workability, mechanical strength, phase assemblage and microstructure properties was investigated using a series of characterization techniques including X-ray diffraction (XRD), thermogravimetric (TG) analysis, Fourier transform infrared spectroscopy (FTIR), N_2 sorption test, mercury intrusion porosimetry (MIP), backscattered electron microscopy (BSEM), energy dispersive X-ray (EDX), workability tests and mechanical strength tests. The findings of this study provide insights into phase transformation and microstructure evolution induced by WG at elevated temperatures, thereby supporting the promising utilization of WG as an effective precursor for developing fire-resistant AAMs.

2. Materials and methods

2.1. Materials

Class F fly ash (FA, purchased from BauMineral GmbH, Germany), ladle slag (LS, provided by TATA steel, the Netherlands) and waste glass (WG, sourced from Maltha, the Netherlands) were utilized as raw materials in this study. The received LS was first dried at 105 °C for 24 h to remove free moisture and subsequently milled for 5 min and the received WG was also ground for 5 min using a ball mill. The particle size distribution of milled raw materials analyzed by a laser particle size analyzer (Mastersizer 2000) is shown in Fig. 1. The average particle size (d50) of FA, LS and WG are 16.57 μm, 12.69 μm and 32.29 μm, respectively. The morphology of the raw materials is illustrated in Fig. 2, the FA particles exhibit a spherical shape whereas the LS and WG particles are irregular. X-ray fluorescence spectrometry (XRF, PANalytical Epsilon 3) was used to characterize the chemical composition of raw materials, and the results are presented in Table 1. The mineral composition of raw materials, determined by X-ray diffraction (XRD, Bruker D6 phaser) is shown in Fig. 3. The XRD pattern of WG exhibits a broad hump between 20° and 40°, similar to that of FA, indicating the presence of amorphous phases. Additionally, quartz, mullite, hematite and magnesioferrite are detected in FA. In LS, the primary crystalline phases identified include hydrogarnet, periclase, mayenite, portlandite, tricalcium aluminate, magnetite and gypsum. The corresponding #PDF-references are shown in Table 2. The analytical level sodium hydroxide pellets and commercial sodium silicate solution (27.69 wt% SiO_2, 8.39 wt% Na_2O, 63.9 wt% H_2O) were applied to prepare the activator.

2.2. Sample preparation

Based on our previous study [15], the activator was prepared by mixing sodium hydroxide pellets, sodium silicate solution and distilled water with a silicate modulus of 1.5 and an equivalent Na_2O% of 6 wt%. The obtained solution was cooled for 24 h to room temperature prior to use. The detailed mix proportions are listed in Table 3. The content of LS was fixed at 10 wt%, and the WG was incorporated at 0%, 10%, 20%, 30%, 40% by mass of the binder. The ratio of water to binder was kept constant at 0.4, in which the water content in sodium silicate solution was included.

All paste samples were prepared using a 5 L Hobart mixer. Firstly, the precursors were dry mixed for 60 s to achieve a homogeneous state.

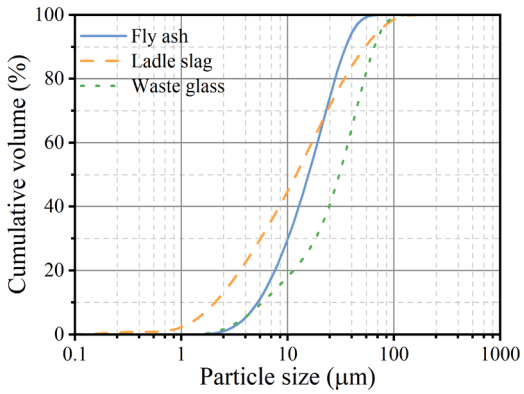

Fig. 1. Particle size distribution of raw materials.

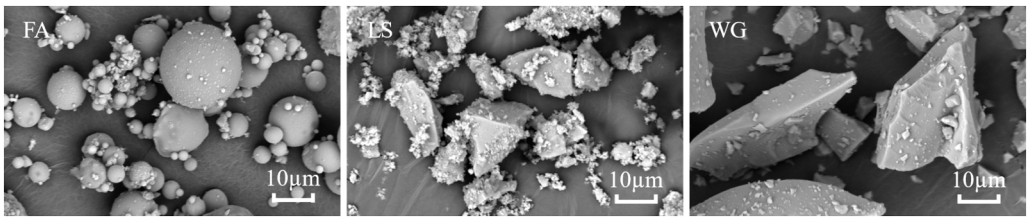

Fig. 2. Morphology of raw materials.

Table 1
The chemical composition of raw materials (wt%).

Oxides	FA	LS	WG
Na_2O	/	/	22.07
MgO	0.98	2.99	1.23
Al_2O_3	24.65	25.98	1.87
SiO_2	52.89	1.72	62.27
P_2O_5	0.63	/	/
SO_3	0.90	0.97	0.10
K_2O	2.36	0.05	0.68
CaO	4.97	56.86	10.81
TiO_2	1.55	0.42	0.10
MnO	0.05	0.42	0.02
Fe_2O_3	8.98	2.60	0.35
Others	0.40	0.16	0.18
LOI	1.65	7.84	0.34

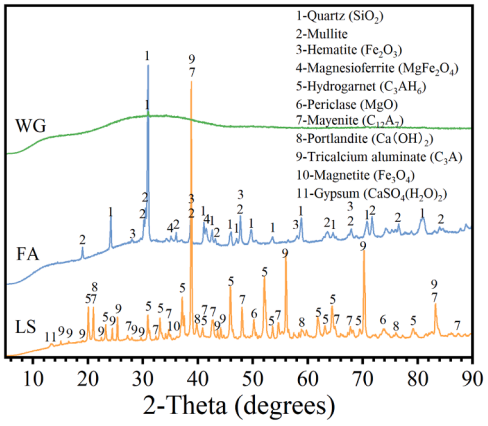

Fig. 3. XRD patterns of raw materials.

Subsequently, the mixture was stirred for 30 s at a low speed with the incorporation of the activator, and then manually scraped from the sides and bottom of the mixing bowl for 30 s to remove adhering paste, and the mixture was further mixed for another 60 s at a high speed. Thereafter, the fresh paste was casted into plastic molds of $40 \times 40 \times 160$ mm^3 and vibrated for 60 s. All specimens were sealed with plastic film and cured at room temperature (20 °C) for 24 h, followed by additional 24 h at 60 °C. Subsequently, the hardened samples were demolded and cured at room temperature under sealed conditions until 28 days.

To stop hydration reaction inside the samples, the hardened pastes were crushed into small particles, immersed into isopropanol for 3 days to terminate hydration, and subsequently dried at 40 °C for 24 h. The dried particles were then grounded into powder (under 80 μm) for further analysis.

2.3. Thermal exposure procedure

In this work, the same elevated exposure procedure was adopted based on our previous study [26]. After 28 days of curing, the samples were placed in a muffle oven, heated from room temperature to target temperatures (400 °C, 600 °C, 800 °C) with a constant heating rate of 10 °C/min, followed by a 1 h dwell at the target temperature, and then naturally cooled down to room temperature for further testing.

Table 2
The structural data of crystalline phases used for XRD/QXRD analysis.

Phase	#PDF-reference
Quartz (SiO_2)	01–086–1560
Mullite ($Al_{2.272}O_{4.864}Si_{0.728}$)	01–083–1881
Hematite (Fe_2O_3)	01–073–2234
Magnesioferrite ($MgFe_2O_4$)	01–089–3084
Hydrogarnet (C_3AH_6)	01–084–1354
Periclase (MgO)	01–074–1225
Mayenite ($C_{12}A_7$)	01–070–2144
Portlandite ($Ca(OH)_2$)	00–004–0733
Tricalcium aluminate (C_3A)	00–038–1429
Magnetite (Fe_3O_4)	01–089–0950
Gypsum ($CaSO_4(H_2O)_2$)	01–076–1746
Nepheline ($NaAlSiO_4$)	00–035–0424
Gehlenite ($Ca_2Al(AlSi)O_7$)	01–089–5917
Albite ($K_{0.2}Na_{0.8}AlSi_3O_8$)	01–083–2215
Wollastonite ($CaSiO_3$)	01–076–0186
Cristobalite (SiO_2)	01–077–1317
Devitrite ($Ca_3Na_2Si_6O_{16}$)	01–077–0410
Grossular ($Ca_3Al_2Si_3O_{12}$)	01–073–2372
Leucite ($KAlSi_2O_6$)	01–071–1147
Anatase (TiO_2)	01–075–1537

Table 3
Mix design of the paste samples (g).

Sample	FA	WG	LS	NaOH	Waterglass	Water
WG0	90.0	/	10.0	4.3	31.5	19.9
WG10	80.0	10.0	10.0	4.3	31.5	19.9
WG20	70.0	20.0	10.0	4.3	31.5	19.9
WG30	60.0	30.0	10.0	4.3	31.5	19.9
WG40	50.0	40.0	10.0	4.3	31.5	19.9

2.4. Methodology

2.4.1. Workability

The fluidity of geopolymer paste was determined by a mini-slump test with a smooth glass and a Hägermann cone (height: 60 mm, base diameter: 100 mm, top diameter: 70 mm). Although the test is widely used, no standardized procedure is currently available for paste mini-slump testing. Therefore, this work the experimental procedure adopted in this study was based on previous studies [27,28]. The fresh paste was placed into the cone and allowed to spread freely for 60 s after raising the cone. Two perpendicular diameters were measured and the average value was calculated.

2.4.2. Compressive strength

The compressive strength of the samples at 7 and 28 days were determined according to EN 196–1. A loading rate of 2400 N/s was applied to all samples, and the average strength value was recorded through triplicate tests.

2.4.3. Phase assemblage

The X-ray diffraction (XRD) test was carried out on the Bruker D6 Phaser instrument equipped with Co-Kα radiation (20 kV, 5 mA). The samples were conducted over a 2θ range from 5° to 90°, with a step size of 0.02° and a counting time of 0.25 s per step. For quantitative X-ray diffraction (QXRD), silicon powder (10 wt%, Siltronix) was added to the samples as an internal standard. All samples were ground by an XRD mill at level 3 speed for 5 min to ensure homogeneity. Rietveld analysis was performed using TOPAS software (version 5.2, Bruker).

The thermogravimetry (TG) test was conducted using the TG 209 Tarsus instrument (Netzsch). The samples were heated from 40 °C to 950 °C at a heating rate of 10 °C/min under a N_2 atmosphere.

The Fourier transform infrared spectroscopy (FTIR) was performed using the Varian 3100 instrument with the wavelength range of 4000–400 cm^{-1} and the resolution of 1 cm^{-1}.

2.4.4. Microstructure characterization

The N_2 sorption test was conducted by using a TriStar II 3020 (Micromeritics) analyser. The powder samples were dried at 40 °C for 2 h prior to testing. The pore size distribution was determined from the adsorption branch using the Barett-Jonyer-Halenda (BJH) method.

The pore structure of particle samples (2–4 mm) was evaluated using mercury intrusion porosimetry (MIP) analysis with the AutoPore IV 9500 (Micromeritics), operating within a pressure range from 0 MPa to 228 MPa. The contact angle between the mercury and the pore surface was 130° and the surface tension of mercury was 0.485 N/m.

The morphology change and phase composition were characterized by backscattered electron microscopy with energy dispersive X-ray (BSEM-EDX) using the PhenomProX (Thermo Fisher Scientific). The measurements were conducted in a backscattered electron mode with the accelerating voltage of 15 kV and a working distance between 7 and 9 mm. The magnifications were 1500 × and 5000 × for BSE images and EDX test, respectively. Before the BSEM test, the samples experienced vacuum impregnation with resin using the CitoVac (Struers), followed by grounding and polishing with Tegramin-30 (Struers), and then the polished surface was coated with Au by a sputter coater (150TS plus, Quorum).

3. Results

3.1. Workability

The results of flow diameter readings, as shown in Fig. 4, illustrated that the substitution of WG increased the fluidity of the mixture within the tested range. The paste without WG exhibited a fluidity of 269.0 mm, and the fluidity showed a nearly linear rise with increasing WG content, reaching a maximum flow diameter of 344.3 mm at WG40, which was 28% higher than WG0. It should be noted that the workability of the paste was influenced by several competing factors. On the one hand, the angular morphology of WG particles increased the interparticle friction and diminished the ball-bearing effect of spherical FA particles, thereby reducing the workability [29]. On the other hand, WG particles exhibited low water absorption property, resulting in more free water being available in the mixture and thus improving workability [17,30,31]. Moreover, the inherently hydrophilic surface of WG particles promoted their wetting and dispersion in alkaline solutions, which might contribute to a more homogeneous particle distribution and enhanced workability [32]. Therefore, the positive effects of WG on water availability and particle dispersion dominated, leading to an overall increase in workability.

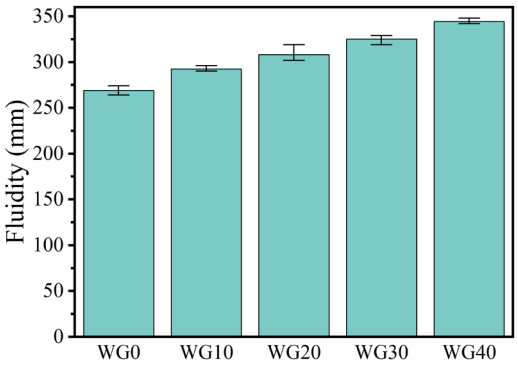

Fig. 4. Fluidity of the pastes with different WG substitutions.

3.2. Compressive strength

The compressive strength results at 7d and 28d for different substitution of WG are presented in Fig. 5. A decreasing trend was observed with the increasing WG content at both ages. The 7d and 28d compressive strength of WG0 are 11.35 MPa and 13.73 MPa, which are 43% and 50% higher than those of WG40, respectively. The reduction in compressive strength could be associated with the declined pozzolanic reactivity of precursors and weakened interface when FA was replaced by WG [17]. The reactivity of WG was lower than that of FA owing to its larger particle size, which limited the formation of geopolymeric gels [33]. In addition, the irregular morphology of WG particles disrupted the interfacial bonding with matrix, thereby resulting in a looser microstructure [30]. Therefore, these chemical and physical changes ultimately resulted in a decrease in compressive strength.

3.3. Hydrates and microstructure

Fig. 6 exhibits the XRD/QXRD results of the samples with different WG content at the age of 28 days. As shown in Fig. 6a, there was no new crystalline phase detected in all samples and the main identified crystalline phases were quartz (SiO_2), mullite ($Al_{2.272}O_{4.864}Si_{0.728}$), hematite ($Fe_2O_3$), hydrogarnet ($C_3AH_6$), mayenite ($C_{12}A_7$), tricalcium aluminate (C_3A) and magnesioferrite ($MgFe_2O_4$). The presence of C_3A and $C_{12}A_7$ suggested that the LS was not fully reacted. Meanwhile, it could be observed that the intensities of the quartz and mullite peaks decreased, while the broad hump from 25° to 40° became more pronounced with the increasing WG content. This was mainly because WG is composed predominantly of amorphous phases, with negligible crystalline components (Fig. 3), whereas FA contains detectable crystalline phases such as quartz and mullite. Therefore, according to the QXRD results (Fig. 6b), the content of quartz and mullite in the system gradually decreased with the increasing WG, whereas the amorphous phase content showed an increasing trend. The increase in amorphous phase was primarily attributed to the inherent higher amorphous nature of WG, rather than to the increased gel formation.

The TG/DTG results of all samples are presented in Fig. 7. The

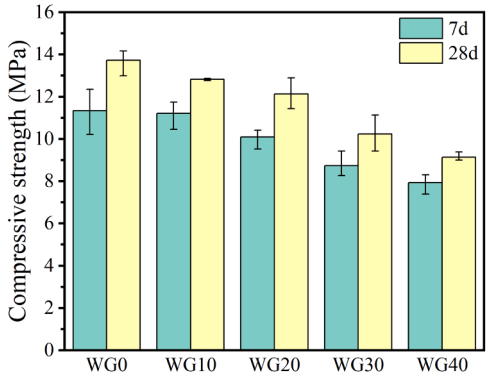

Fig. 5. 7d and 28d compressive strength of the pastes with different WG content.

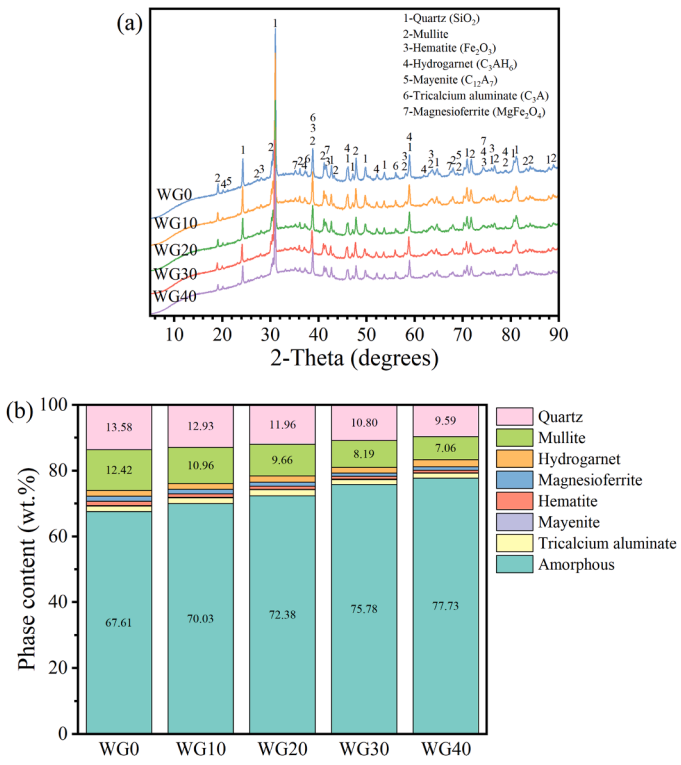

Fig. 6. (a) XRD patterns and (b) quantitative phase composition of the samples at 28 days.

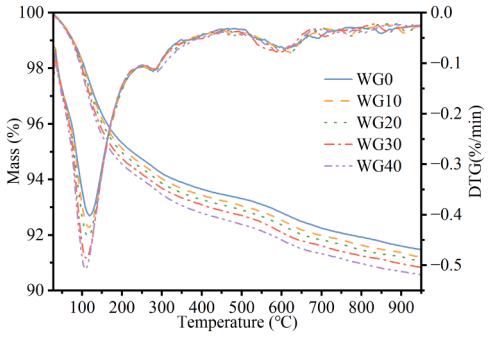

Fig. 7. TG/DTG analysis of the pastes with different WG content.

samples showed greater mass loss with the increased incorporation of WG. According to the DTG curves, three mass loss peaks were observed in the range of 40–200 °C, around 300 °C, and 500–700 °C, respectively. The first peak (40–200 °C) was mainly attributed to the release of bonded water from gels products [34,35]. The second peak near 300 °C was due to the dehydration of hydrogarnet, which was detected in the XRD patterns [15]. In addition, the broad peak (500–700 °C) was ascribed to the decomposition of carbonated phases [7]. Notably, the main mass loss peak gradually shifted from 118 °C for WG0 to 108 °C for WG40 with the increment of WG content, which might suggest the formation of gels with more loosely bonded water [4]. As reported in reference [4], the loss of bound water from C–A–S–H gel occurs at around 108 °C while that from N–A–S–H gel occurs at approximately 128 °C. Consequently, the increased intensity and leftward shift of the peak might be associated with the additional formation of C–(A)–S–H gel, owing to the higher Ca content induced by the incorporation of WG.

Fig. 8 demonstrates FTIR spectra of raw materials and samples with different WG content. For raw LS, the peaks observed at 3659 cm^{-1} and 1407 cm^{-1} were attributed to O–H stretching vibration and O–C–O vibration of carbonate groups [36], respectively. The peaks in the range of 900–700 cm^{-1} and at 515 cm^{-1} corresponded to Al–O bonds in calcium aluminates and the symmetric stretching vibration of Al–O–Al bonds [15]. FA exhibited a main peak at 1024 cm^{-1} due to the Si–O–T asymmetric stretching vibration, where T represented the Si or Al units. The peaks between 800 cm^{-1} and 650 cm^{-1} were from the Si–O stretching vibrations in quartz [37], and the peak around 435 cm^{-1} was assigned to the Si–O symmetric vibration in vitreous silica [38]. Similarly, the raw WG showed characteristic peaks at 989 cm^{-1} , 768 cm^{-1} , and 435 cm^{-1} , corresponding to the asymmetric stretching, symmetric stretching, and bending vibrations of Si–O–Si bonds, respectively [39]. Furthermore, no significant differences were observed among the samples from Fig. 8b. Most peaks remain similar except for the asymmetric stretching of Si–O–T bonds. The band at 988 cm^{-1} in the WG0 sample slightly shifted to 983 cm^{-1} with the addition of WG. Given that the addition of WG increased Ca content while reducing Al content, this shift was more likely due to the disruption of the Si–O–T bonds by the introduced Ca [4, 37,40]. The disruption generated more non-bridging oxygens, thus promoting the formation of C–(A)–S–H gel, which was in line with TG results.

The cumulative pore volume of all samples in the range of 2–150 nm by N_2 sorption test are exhibited in Fig. 9a. The cumulative pore volume decreased from 0.073 cm^3 /g to 0.0524 cm^3 /g with increasing WG content. It was observed that the reduction was primarily concentrated in the pore size range below 30 nm, indicating that the main changes were associated with gel pores (<10 nm) and transition pores within the 10–30 nm range. As shown in Fig. 9b, the gel pore volume progressively decreased with the incorporation of WG. This could be explained by the lower pozzolanic activity of WG, which reduced the gel formation, since gel pore volume was closely related to the amount of gel products at ambient temperature [41]. Furthermore, a critical WG content was

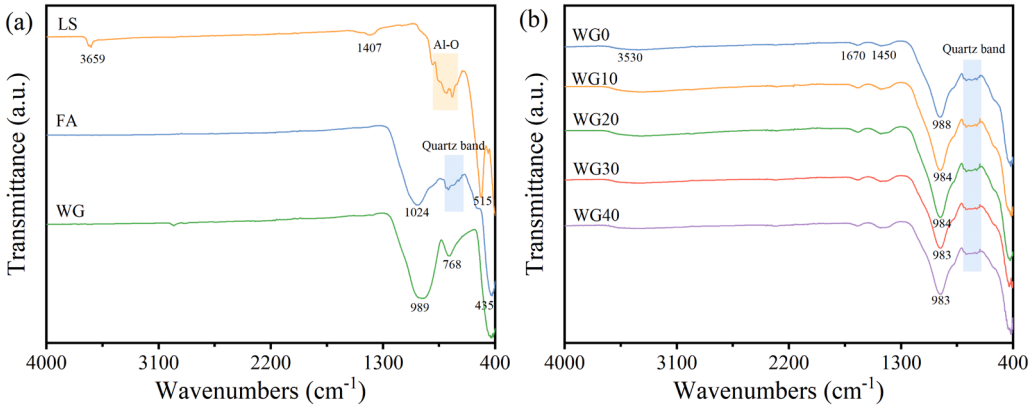

Fig. 8. FTIR spectra of (a) raw materials and (b) the pastes with different WG content.

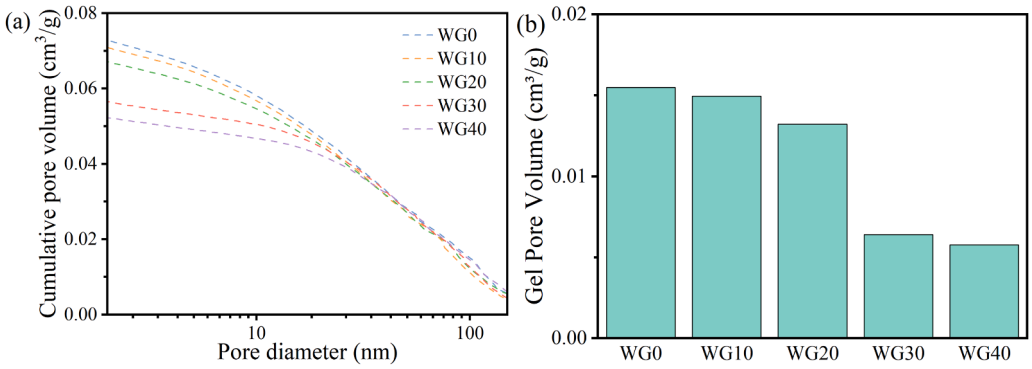

Fig. 9. (a) BJH cumulative pore volume and (b) gel pore volume of the pastes with different WG content.

observed as a significant reduction occurred when the WG content exceeded 20%.

In order to better understand the effect of WG content on pore structure, MIP test was conducted to analyze the porosity and pore distribution, and the results are demonstrated in Fig. 10 and Table 4. The pore distribution exhibited similar trends across different WG replacement levels, with the porosity and the critical pore diameter remaining around 35% and 62.50 nm, respectively. This indicated that the addition of WG had limited effect on porosity and pore connectivity. In addition, the pore volume fraction of all samples was shown in Fig. 10b. Generally, pores in cementitious materials can be classified into 4 types: gel pores (<10 nm), transitional pores (10–100 nm), capillary pores (100–1000 nm), macropores (>1000 nm). Here, the increased fraction of macropores might be attributed to the weakened interface caused by the incremental addition of WG, even though the improved workability could facilitate the release of entrapped air bubbles, partially offsetting the increase. For the pores smaller than 1000 nm, a threshold content of WG was also observed at 20%, which is in good agreement with the N_2 sorption findings. When the substitution level was less than 20%, the incorporation of WG reduced the proportion of capillary pores and barely affected that of transitional pores. However, at a higher level (>20%), a reversed trend with an increase in capillary pores and a decline in transitional pores was observed. The results were consistent with the changes in average pore diameter, which indicated that a low replacement ratio of WG could refine the pore size, whereas a higher ratio tended to coarsen it.

Overall, adding WG enriched the amorphous phases content and promoted the formation of C-A-S-H gels owing to the intrinsic properties of WG. Although the total porosity is largely unchanged, higher WG incorporation led to a coarser microstructure with an increased fraction of macropores.

Table 4
Pore parameters of the pastes with different WG content.

	WG0	WG10	WG20	WG30	WG40
porosity (%)	35.16	35.48	35.13	34.43	34.61
critical pore diameter (nm)	62.49	62.50	62.50	62.52	62.51
average pore diameter (nm)	46.30	46.20	44.60	50.00	52.60
cumulative intrusion (mL/g)	0.2848	0.2812	0.2759	0.2677	0.2687

3.4. High temperature resistance

3.4.1. Thermal mechanical properties

The 28d compressive strength results and residual strength ratios under high temperature exposure are presented in Fig. 11. It was observed that all samples exhibited an improvement in compressive strength when the temperature was below 600 °C. Moreover, the 20% WG threshold was further validated in this ternary system as the temperature increased. At 800 °C, the WG0, WG10 and WG20 samples exhibited superior performance with WG10 and WG20 showing markedly higher compressive strength than WG0. As shown in Fig. 11b, the compressive strength of WG10 and WG20 were 2.52 and 2.57 times greater than their respective values at ambient temperature. In contrast, the samples with 30% WG and above suffered a significant decline in compressive strength, although their strength remained higher than that at ambient temperature. Hence, to further investigate the underlying mechanisms governing the strength enhancement at moderate WG content and the deterioration at higher content under elevated temperatures, WG0, WG20 and WG40 were selected for subsequent experiments and in-depth analysis.

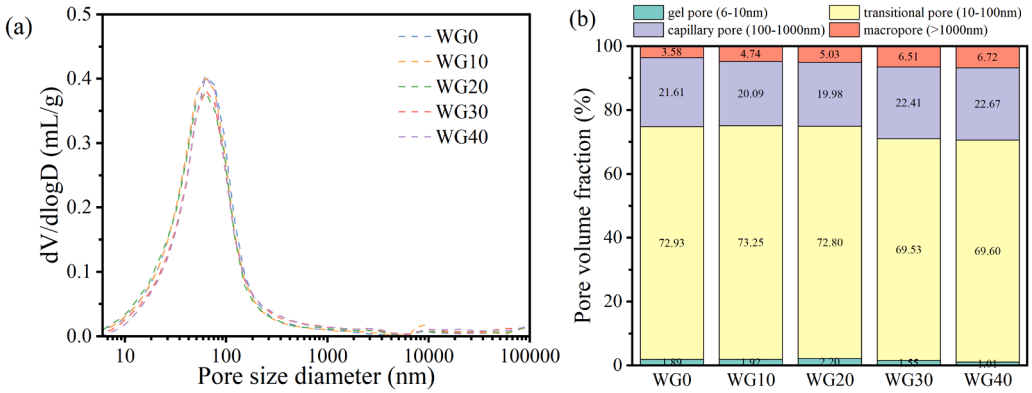

Fig. 10. (a) Pore size distribution and (b) pore volume fraction of the pastes with different WG content.

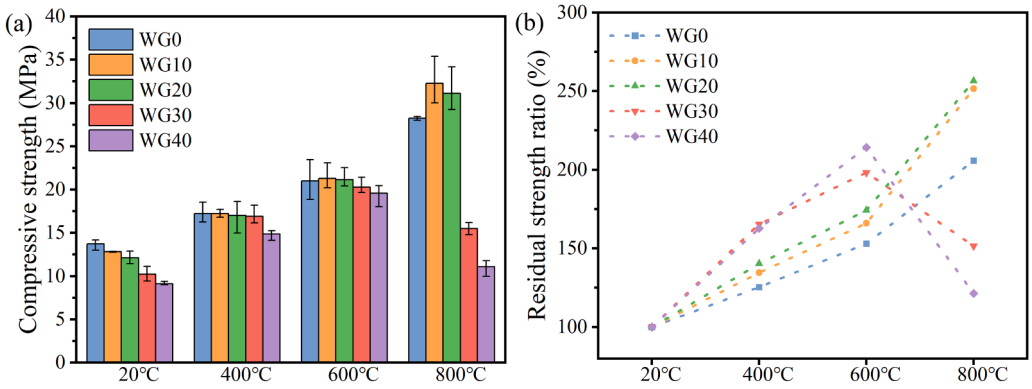

Fig. 11. (a) 28d compressive strength and (b) residual strength ratio of the pastes at elevated temperatures.

3.4.2. *Phase transformation*

Fig. 12 illustrates the XRD patterns of the samples exposed to different temperatures. As the temperature increased to 400 °C, the peaks corresponding to hydrogarnet disappeared, which could be attributed to the dehydration of hydrogarnet occurring around 300 °C [15], consistent with TG results. Futhermore, no additional crystalline phases were detected at 600 °C. However, after heating to 800 °C, several new crystalline phases emerged, including nepheline ($NaAlSiO_4$), gehlenite ($Ca_2Al(AlSi)O_7$), albite ($K_{0.2}Na_{0.8}AlSi_3O_8$) and wollastonite ($CaSiO_3$). At 800 °C, the nepheline and gehlenite phases originated from the decomposition and recrystallization of N–A–S–H gel and C–(A)–S–H gel, respectively. The appearance of albite was associated with the transformation of N–K–A–S–H gel, suggesting that sodium in N–A–S–H gel was partially replaced by pottasium [8,16,42]. Interestingly, the formation of wollastonite is not only from the recrystallization of C–(A)–S–H gel, but also from that of raw WG when exposed to high temperatures. As shown in Fig. 13, the main composition of raw WG remained in the amorphous phase at 600 °C, whereas many crystalline phases emerged as the temperature increased to 800 °C with wollastonite accounting for 13.344% (Table 5).

To further investigate the changes of amorphous and crystalline phases in the pastes, QXRD analysis combined with TG results was conducted and the result is presented in Fig. 14. The total phase content does not reach 100% after heating due to mass loss associated with dehydration and decomposition of the components in the pastes, as evidenced by TG analysis. In accordance with the XRD pattern in Fig. 12a, hydrogarnet disappeared after exposure to 400 °C and was transformed into calcium aluminate, whose content exhibited a slight increase across all samples [15]. Moreover, the amorphous phase content decreased at 400 °C due to dehydration of the gel products, and then remained stable as the temperature increased to 600 °C. At 800 °C, it could be observed that new crystalline phases emerged and the WG

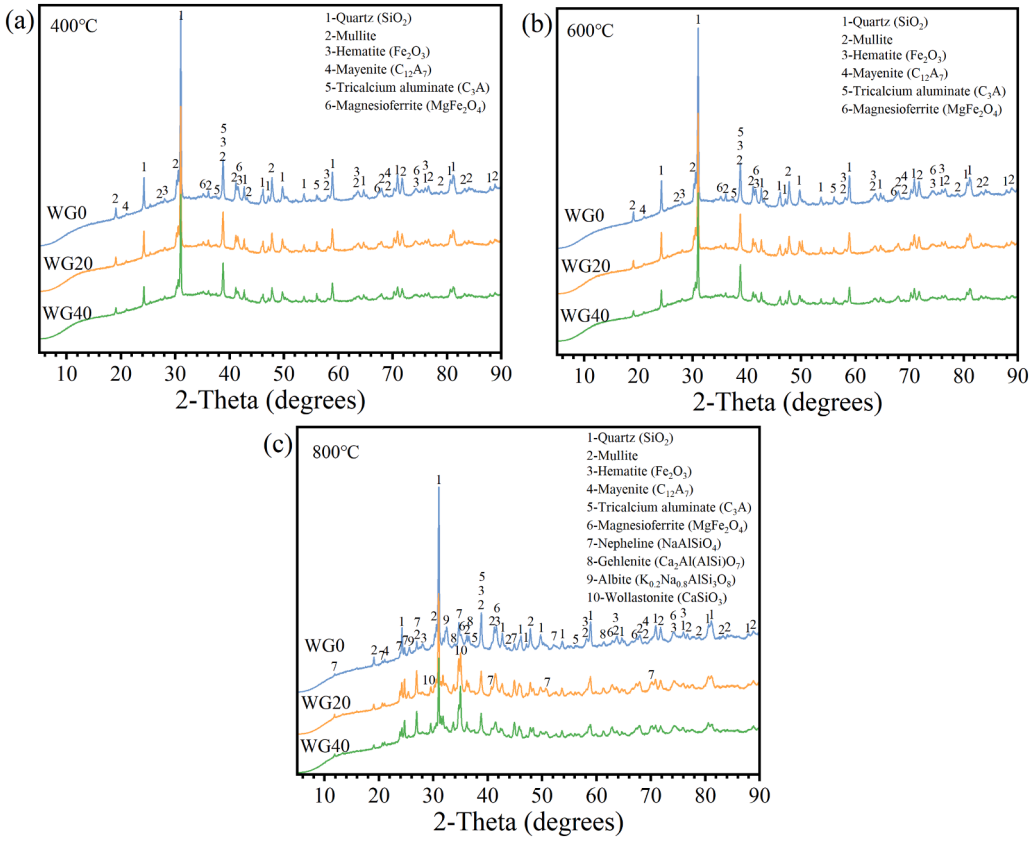

Fig. 12. XRD patterns of the samples at (a) 400 °C, (b) 600 °C and (c) 800 °C.

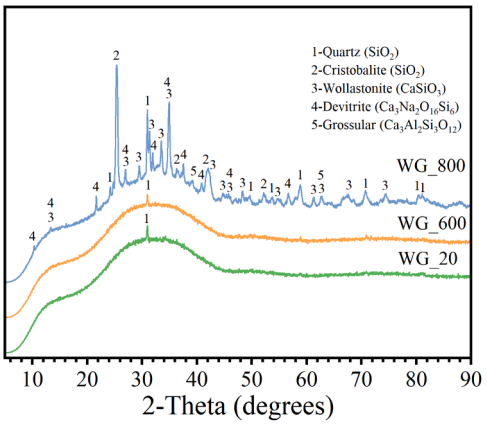

Fig. 13. XRD patterns of raw WG under high temperatures.

Table 5
QXRD results of raw WG at 800 °C.

Phase Name	Weight percentage (wt%)
Quartz (SiO_2)	2.89
Cristobalite (SiO_2)	9.50
Wollastonite ($CaSiO_3$)	13.34
Devitrite ($Ca_3Na_2Si_6O_{16}$)	11.64
Grossular ($Ca_3Al_2Si_3O_{12}$)	0.79
Leucite ($KAlSi_2O_6$)	0.70
Anatase (TiO_2)	0.48
Amorphous	60.66

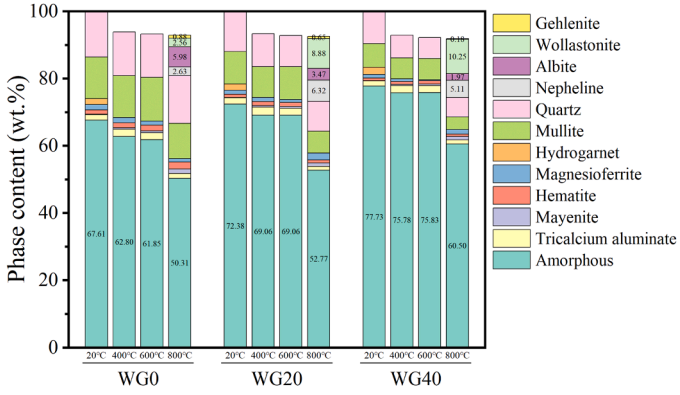

Fig. 14. Quantitative phase composition of the samples at elevated temperatures.

content significantly influenced their formation. Compared to the sample without WG, the samples containing WG exhibited a greater reduction in amorphous phase content and a more pronounced increase in newly formed crystalline phases. As the WG replacement level increased, the K content in the system decreased, in line with the gradual reduction in albite content. Meanwhile, the nepheline content also formed from N–A–S–H gel exhibited a significant increase in WG20, followed by a slight decrease in WG40. Additionally, the gehlenite content was limited across all samples while wollastonite increased markly with higher WG incorporation. As mentioned above, the variation of wollastonite could be attributed to two reasons. On the one hand, the recrystallization of residue WG contributed to the increase of wollastionite. On the other hand, the introduction of additional Ca, Si, and Na by WG, along with a relative reduction in Al and K content derived from FA, promoted the formation of C–(A)–S–H gel. Therefore, more crystalline phases associated with C–(A)–S–H were formed in the samples contaning WG.

The FTIR spectra of WG0, WG20 and WG40 samples at different temperatures are compared in Fig. 15. The O–H bonds vibration at 3530 cm^{-1} and 1654 cm^{-1} disappeared when the temperature was elevated to 400 °C, which was attributed to the loss of phsically absorbed and chemically bonded water. Similarly, the peak near 1450 cm^{-1} disappeared after exposure to 600 °C due to the decomposition of carbonates, in alignment with the TG results. However, the quartz band around 800–650 cm^{-1} exhibited negligible changes owing to the thermal stability of quartz sourced from FA, as confirmed by the XRD results. Notably, for the samples without WG, the Si–O–T band shifted from 988 to 983 cm^{-1} as the temperature increased, indicating that high temperature promoted the substitution of Si by Al within the aluminosilicate gel network [4]. Similar shifts were observed in WG20 and WG40 samples at temperatures below 600 °C, which might be attributed to the breakage of bridging oxygen bonds induced by the Ca^{2+} release. Upon further heating to 800 °C, the previously overlapping band transformed into three distinct peaks, with one appearing at a higher wavenumber and the other two at lower wavenumbers. The peak near 962 cm^{-1} was attributed to the asymmetric stretching vibrations of Si–O bonds in C–(A)–S–H gels [43,44], while the peak at around 999 cm^{-1} was associated with the asymmetric Si–O–T stretching in N–A–S–H gels [45,46], implying that the geopolymeric reaction was still ongoing as the temperature increased. In addition, the peak at 904 cm^{-1} corresponded to asymmetric vibrations of terminal Si–O bonds in wollastonite phase [45,47,48], which indicated that more wollastonite formed in the sample containing WG.

3.4.3. *Microstructure evolution*

The N_2 sorption results of the samples at elevated temperatures are shown in Fig. 16. At 400 °C, the cumulative pore volume decreased in WG0 and WG20, while WG40 exhibited a slight increase. As the temperature further increased, a pronounced reduction in cumulative pore volume was observed across all samples, reaching the lowest values at 800 °C, indicating the collapse of small pores. From one aspect, geopolymeric reaction continued to produce additional gels as the temperature increased to 400 °C, thus increasing gel pores volume. From another aspect, the dehydration of gel phases led to the collapse of gel pores and subsequent densification of gel structures [49,50]. Hence, the gel pore volume displayed an increase when the gel formation exceeded the gel reduction, as observed in WG40. Conversely, it decreased in WG0 and WG20. Additionally, at 600 °C, the samples containing WG exhibited a greater loss in gel pore volume. This was because the WG addition promoted the increased formation of C–(A)–S–H gels, which are less thermally stable than N–A–S–H gels and therefore underwent more extensive decomposition [8]. After exposure to 800 °C, the recrystallization of gel phases led to a further decrease in gel pore volume, with minimal differences observed among the samples [8].

The MIP results were illustrated in Fig. 17 and Table 6. It was clearly seen that the main peak shifted to the right progressively with increasing temperature, indicating a coarsening trend of the pore size structure across all specimens. As the temperature increased from 20 °C to 400 °C, the main peaks of all samples exhibited slight shifts. The critical pore diameters of WG0 and WG20 remained similar, both around 77 nm, whereas that of WG40 reached 95.31 nm. At this stage, the dominant pore type was transitional pore, but its proportion decreased with increasing WG content, accompanied by a corresponding rise in the fraction of capillary pore. The enlargement in pore size could be attributed to the evaporation of free and bounded water, which contributed to the vapor pressure buildup and the initiation of microcracks [51,52].

Moreover, the samples containing WG exhibited higher water content, as indicated by TG results, which might have intensified the deterioration of the pore structure. At 600 °C, the critical pore diameter further increased, and capillary pore accounted for the largest proportion

of the total pore volume in the system, suggesting extensive collapse

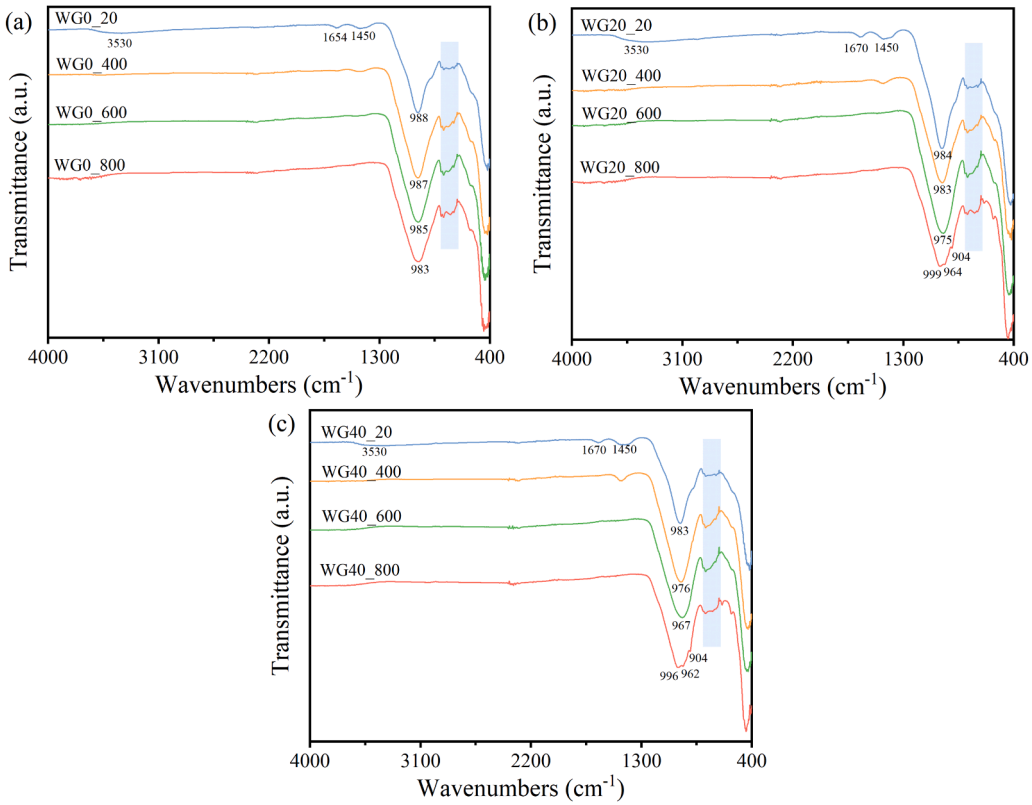

Fig. 15. FTIR spectra of (a) WG0, (b) WG20 and (c) WG40 at elevated temperatures.

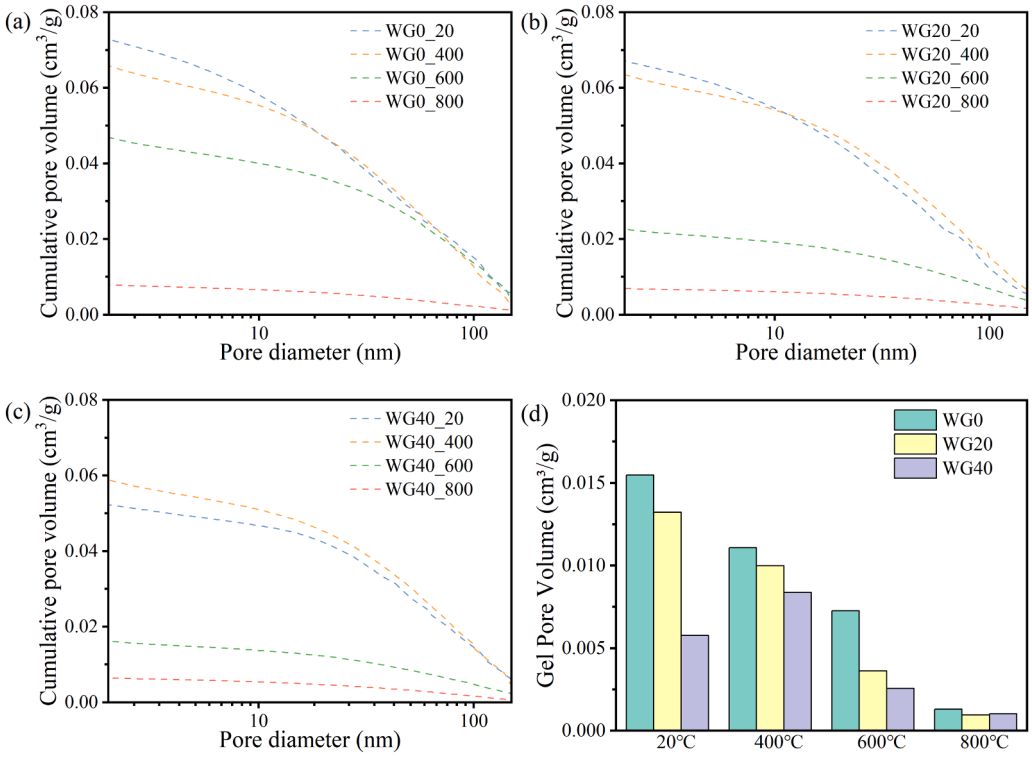

Fig. 16. (a-c) BJH cumulative pore volume of WG0, WG20, and WG40, and (d) gel pore volume of the samples at elevated temperatures.

of smaller pores and continued propagation of microcracks, as supported by BET results. When the temperature was

elevated to 800 °C, the decomposition and recrystallization of gel phases led to a further increase in pore size [8]. Nevertheless, viscous sintering reaction took place in the matrix and WG particles melted, which contributed to healing small pores and microcracks [15,17]. In

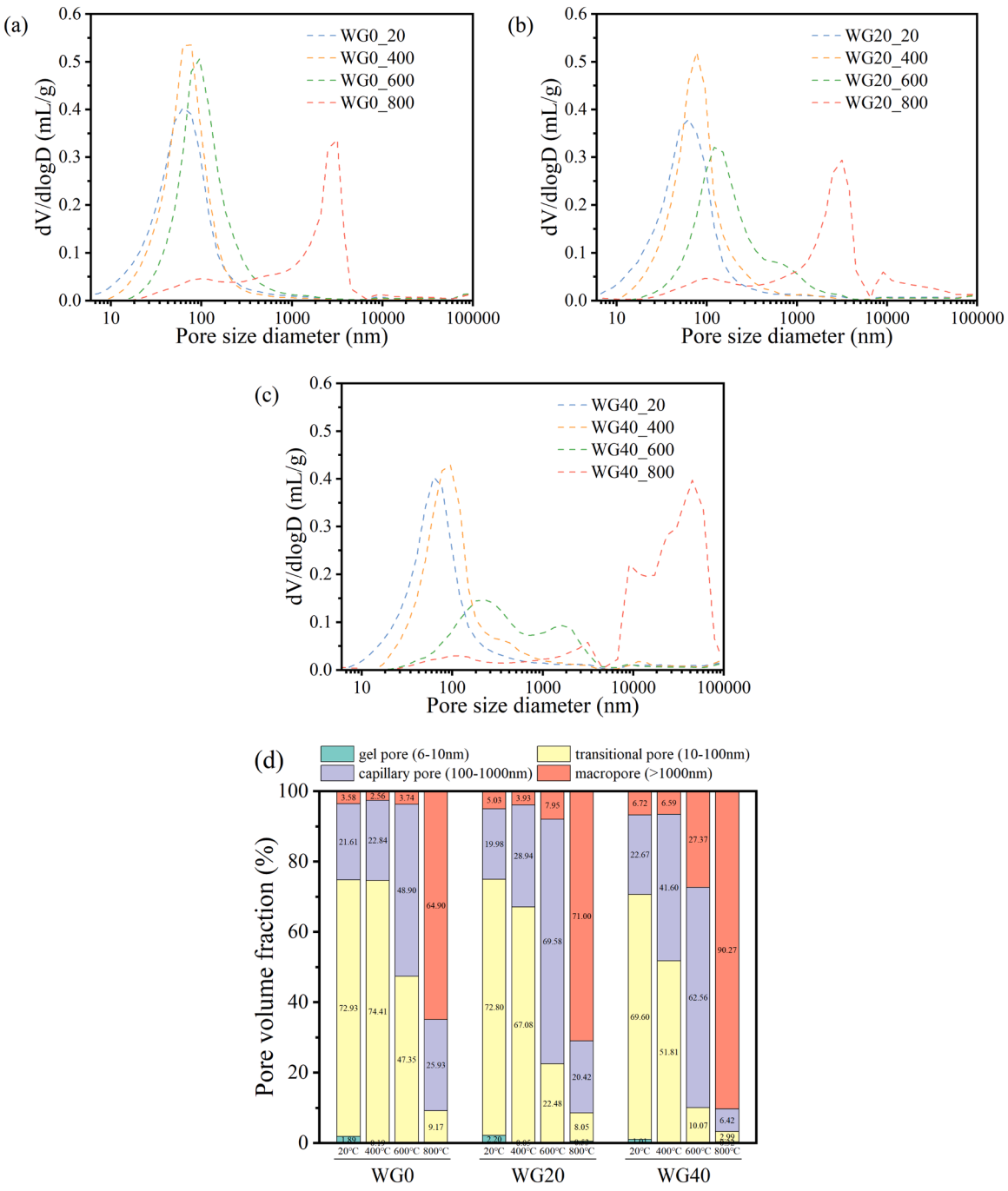

Fig. 17. (a-c) Pore size distribution of WG0, WG20, and WG40, and (d) pore volume fraction of the samples at elevated temperatures.

parallel, the cracks and pores would further develop due to the increased thermal stress. Consequently, macropore became the dominant pore type in the system. Notably, the WG40 sample exhibited a dramatic increase in pore size, with its critical pore diameter reaching 44762.33 nm — more than ten times larger than that observed in WG0 and WG20. In terms of pore fraction, macropore constituted 90.72% of the total pore volume in WG40, in contrast to 71.00% in WG20 and 64.90% in WG0. This drastic structural change was closely associated with the substantial strength loss observed in WG40 at 800 °C, suggesting that excessive incorporation of WG adversely affected high-temperature pore evolution due to the introduced initial structural defects (Fig. 18) and the potential over-melting of WG.

Fig. 18 illustrates the microstructural evolution of WG0, WG20, and WG40 samples at elevated temperatures. At ambient temperature, many unreacted particles were observed in the matrix. FA and LS particles appeared closely bonded with the surrounding matrix, while cracks and pores were formed around WG particles, indicating that the lower reactivity of WG led to a weaker interface with the matrix, thereby reducing compressive strength. As the temperature increased to 400 °C, crack initiation and propagation occurred along particle boundaries. Compared with the WG0 sample, more pronounced crack development was observed in WG20, whereas WG40 exhibited more pores. When heated to 600 °C, widened cracks, coarser pores, and partial collapse of the matrix were observed. These changes could be attributed to the increased thermal stress as well as the dehydration of gels, which caused the collapse of internal gel pores. Following exposure to 800 °C, the viscous sintering reaction and melted WG rendered the unreacted particle boundaries and cracks no longer visible, accompanied by a highly

Table 6
Pore parameters of the samples with different temperatures.

Sample	Temperature (°C)	porosity (%)	critical pore diameter (nm)	average pore diameter (nm)	cumulative intrusion (mL/g)
WG0	20	35.16	62.49	46.30	0.285
	400	35.92	77.03	57.20	0.293
	600	37.10	95.30	88.30	0.291
	800	27.32	3147.02	329.20	0.189
WG20	20	35.13	62.50	44.60	0.276
	400	37.41	77.04	64.30	0.290
	600	34.29	120.78	129.00	0.244
	800	28.04	3150.72	290.70	0.208
WG40	20	34.61	62.51	52.60	0.269
	400	33.76	95.31	80.90	0.278
	600	26.96	226.28	220.50	0.180
	800	34.32	44762.33	750.60	0.327

porous structure resulting from the gel decomposition and recrystallization [17,26].

To further investigate the gel composition of different samples, at least 80 points from 10 images were selected and the $CaO–SiO_2–Al_2O_3$ ternary diagram was plotted, as shown in Fig. 19. At ambient temperature, most points across all samples clustered in a low-Ca, low-Al, and Si-rich region corresponding to N–(C)–A–S–H gels and the raw WG was also presented. The Ca content in samples containing WG was slightly higher than that in WG0, indicating that the incorporation of WG had a minor influence on the gel composition [4,7]. As the temperature increased to 400 °C, two distinct regions emerged, which implied that the geopolymeric reaction was promoted. In WG0 sample, the distribution of points suggested that the Ca content remained largely unchanged whereas more Al was incorporated into the gel, indicating the formation of an Al-enriched N–(C)–A–S–H phase. In contrast, WG-containing samples exhibited increased levels of both Ca and Al in the reaction products, implying the coexistence of C–(N)–A–S–H and N–(C)–A–S–H gels [7,53]. The decomposition of hydrogarnet provided an additional source of Al, which contributed to the formation of Al-rich gels [15]. Moreover, the addition of WG introduced more Ca into the system, and the higher temperature improved the reactivity of WG, facilitating the release of Ca from WG and resulting in the formation of Ca-rich gels. At 600 °C, the points further shifted toward regions with higher Ca and Al contents, suggesting that more Ca and Al were incorporated into the gel networks, in line with the FTIR results. After exposure to 800 °C, most points in the WG0 sample remained in the N–(C)–A–S–H region, which was consistent with the results in reference [7]. However, the samples containing WG exhibited a broader distribution of points located in both the N–(C)–A–S–H and C–(N)–A–S–H regions, with higher WG dosages corresponding to increased Ca content. These points in the C–(N)–A–S–H region likely represented either residues of incompletely decomposed gel or recrystallized phase, as supported by the XRD results.

4. Discussion

In the present FA–LS–WG system, the amorphous Si-rich phases were mainly derived from raw FA and WG. The reactive Al-rich phases originated from raw FA and LS, whereas the Ca-rich phases were mainly supplied by raw LS, with a minor contribution from WG. Therefore, the phase transformation and pore structure evolution were governed by the combined effects of FA, LS and WG. As this work is developed from our previous FA–LS system, the discussion part focuses on elucidating how WG enhances the fire resistance of the FA–LS matrix.

As demonstrated by the above results, WG significantly influences phase transformation and microstructure evolution, both of which are key factors governing the compressive strength of samples at elevated temperatures. This section will further explore the underlying mechanisms and elucidate the role of WG in the following two stages, as

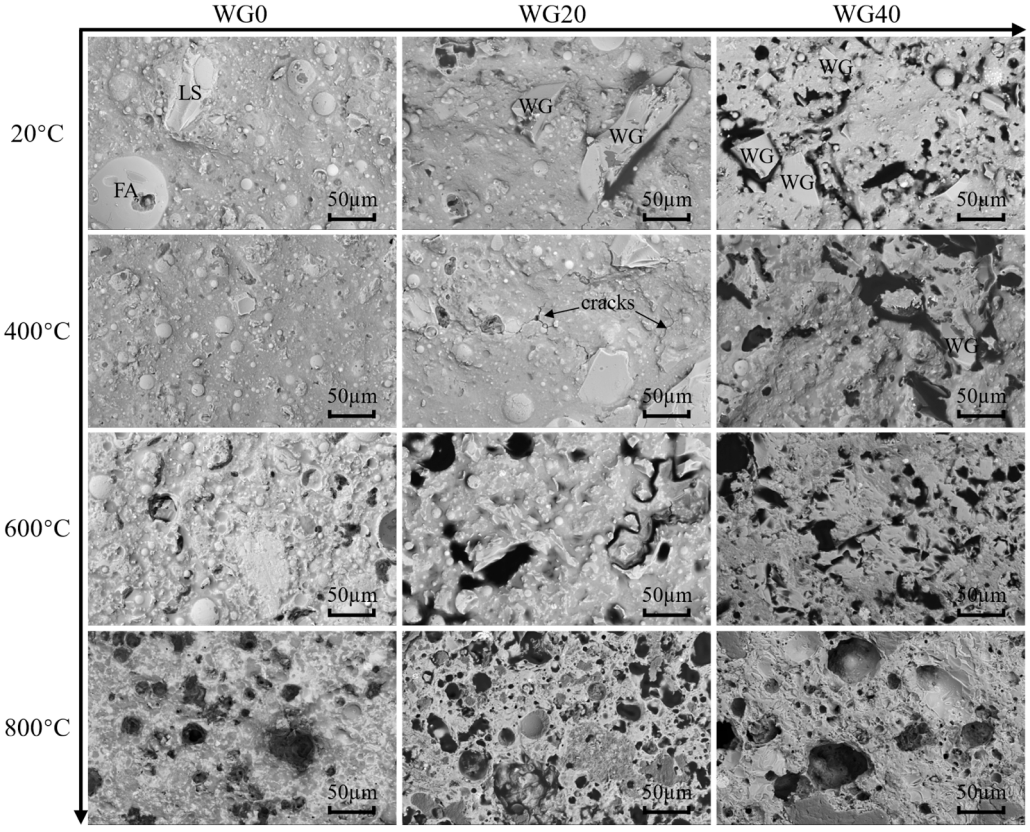

Fig. 18. BSEM images of the samples at elevated temperatures.

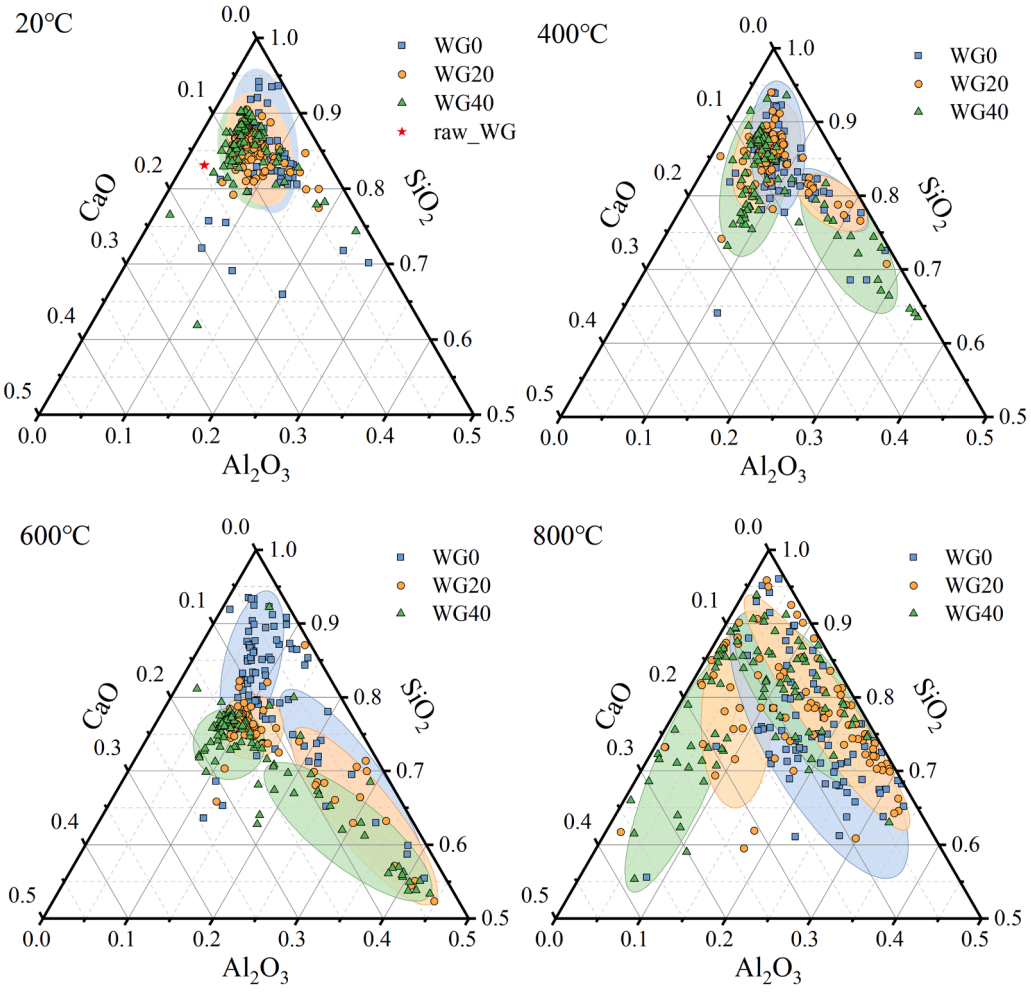

Fig. 19. Composition ternary diagram in $CaO–SiO_2–Al_2O_3$ of the samples at different temperatures.

schematically illustrated in Fig. 21.

4.1. Secondary hydration (20 °C to 600 °C)

At the range from 20 °C to 600 °C, the compressive strength of all samples exhibited an increasing trend with rising temperature. On the one hand, dehydration of the gel phases led to collapse of gel pores, resulting in the formation of larger pores. Moreover, the accumulated vapor pressure and increased thermal stress initiated and propagated cracks, further enlarging pore sizes and hindering strength development [51,52]. On the other hand, the gel structure became more compact when the pores within gel products collapsed, contributing to an increase in micro-mechanical strength of gel phases. The average elastic modulus of reaction products in Class F fly ash-slag hybrid system increased from 27 GPa at ambient temperature to 50.3 GPa and 84.2 GPa after exposed to 400 °C and 600 °C, respectively, as reported in the reference [54]. In addition, the ongoing geopolymerization of residual unreacted precursors supplied new gel phases, which tended to evolve towards Ca-enriched C–(N)–A–S–H gel and Al-enriched N–(C)–A–S–H gel (Fig. 19). Therefore, these factors suggested that the enhancement in compressive strength at the macroscopic scale stems from the strengthening of microscopic gel clusters, along with continued gel formation, which outweighed the detrimental effects of crack propagation and pore coarsening.

With increasing WG incorporation, the composition of crystalline phases remained stable. However, the smaller reduction in amorphous phase content (Fig. 14) and more pronounced peak shifts (Fig. 15) suggested that elevated temperatures enhanced the reactivity of WG and promoted further geopolymerization. Regarding pore structure, the addition of WG led to the coarsening of pore and the effect became more pronounced with high WG content induced by the greater water loss, especially as the temperature rose (Fig. 17). Although the samples containing WG exhibited lower porosity at 600 °C, the fraction of capillary pores and macropores increased significantly, which was harmful to mechanical properties. Hence, a moderate WG amount achieved a balance between the advantages of improved phase assemblage and the drawbacks of pore structure enlargement, resulting in comparable compressive strength. In contrast, excessive WG addition tended to exacerbate pore structure degradation, thereby leading to a relative reduction in compressive strength.

4.2. Recrystallization (600 °C to 800 °C)

The macroscopic appearance and volume evolution of the samples as the temperature rises from 600 °C to 800 °C are shown in Fig. 20. At 600 °C, higher WG content resulted in more visible cracks and greater volumetric shrinkage relative to initial volume, reaching 9.03%, 14.84% and 20.96%, respectively. As temperature increased to 800 °C, both WG0 and WG20 exhibited more cracks and further shrinkage, whereas the volumetric change of WG20 was lower. This suggested that incorporating 20% WG might be beneficial for stabilizing the structure at elevated temperatures. Interestingly, WG40 showed negligible cracking at 800°C, accompanied by significant volumetric expansion. Although the overall shape of WG40 was preserved, its dimensional stability was

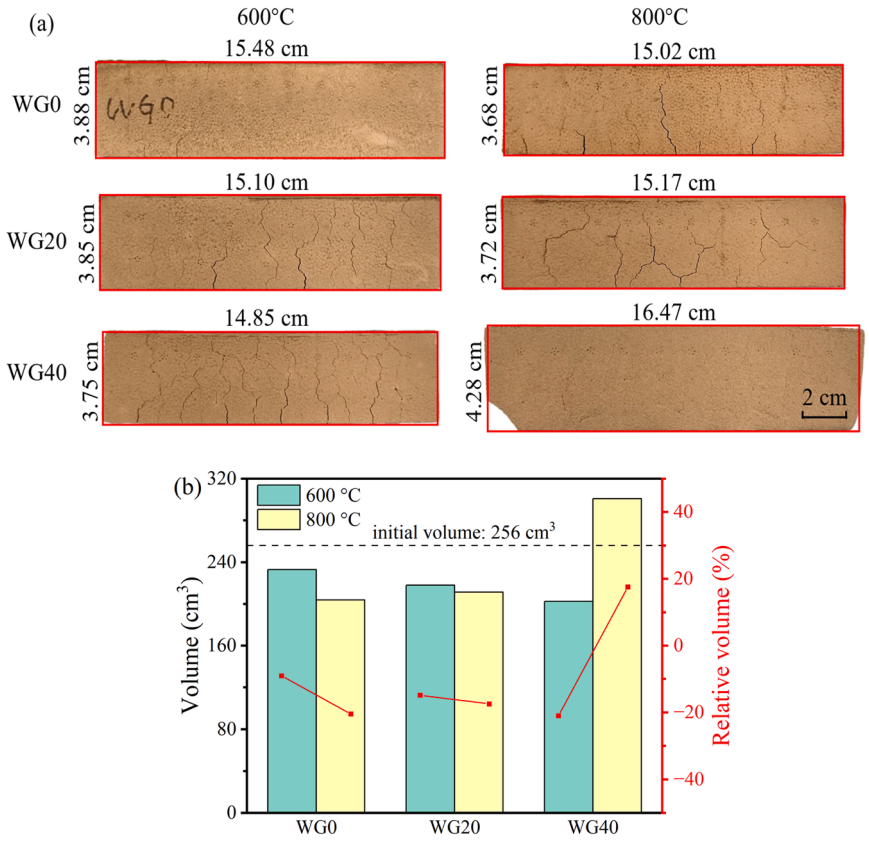

Fig. 20. Changes in appearance and volume of the samples with temperature from 600 °C to 800 °C.

poor, with the relative volume changing from −17.55–17.43% at this stage. These phenomena indicated that the WG content and the physical and chemical transformations of WG played increasingly important roles at higher temperatures.

At this stage, the residue WG partly recrystallized into new crystalline phases, serving as a supplement to those formed from recrystallization of gel products. These newly formed crystalline phases exhibited excellent fire resistance, yet, their excessive formation might disrupt the gel skeleton, contributing to increased pore sizes [55]. In parallel, some physical transformations also played a critical role in altering the pore structure. The geopolymer matrix and the unreacted WG particles achieved their softening points when temperature exceeded 600 °C, indicating the onset of viscous sintering [15,56,57]. Moreover, when the temperature went up to 700 °C, the viscous WG transitioned into a molten state, which healed small pores and microcracks and enhanced the internal cohesion of matrix [17,58]. Overall, recrystallization and viscous sintering played dominant roles in strength development, accompanied by further coarsening of the pore structure and propagation of cracks, as presented in Fig. 21.

However, excessive addition of WG failed to promote the development of compressive strength at 800 °C. In the WG40 sample, molten WG not only filled the micropores and microcracks within the matrix, but also likely flowed to the surface and sealed surface cracks, leading to a crack-free phenomenon. Hence, the volume expansion and large pores formation were attributed to the excessive molten WG, which encapsulated internal gas. Upon heating to 800 °C, the expansion of entrapped gas promoted pore coarsening and macroscopic swelling, as evidenced by MIP results (Table 6) and visual observations (Fig. 20). Similar expansion behavior has been reported in studies on self-foamed glass-ceramics [59]. Moreover, WG40 exhibited more cracks and pores at the initial stage, which exacerbated structural deterioration as the temperature increased (Fig. 18). These factors led to macropores occupying approximately 90% of the pore system. Consequently, the transformation from small pores to large pores and from microcracks to macrocracks compromised the internal structure, significantly reducing the mechanical strength. In contrast, incorporating a moderate amount of WG resulted in a comparable pore structure and integrity. Moreover, it facilitated the increased formation of new crystalline phases, which served as thermally stable aggregates that strengthen the matrix, thereby contributing to strength improvement [15].

5. Conclusions

This work aims to elucidate the underlying mechanisms governing structural evolution in a ternary geopolymer system with varying WG contents under elevated temperatures. The feasibility of utilizing WG as a precursor in AAMs for fire-resistant applications is verified and the role of WG on the phase composition, structural change and mechanical properties after exposure to high temperatures are investigated. Based on the acquired results, detailed conclusions can be drawn as follows:

(1) At ambient temperature, WG improves workability owing to its low water absorption property. Although its relatively low chemical reactivity and poor interfacial bonding result in a decline in compressive strength, WG10 and WG20 still preserve 93.42% and 88.42% of the strength, respectively.
(2) The system contains both N–A–S–H and C–A–S–H gels, and WG addition may promote C-A-S-H gel formation. Moderate content of WG (<20%) does not significantly alter the pore system, as the gel pore volume only slightly decreases from 0.0155 cm^3 /g to 0.0132 cm^3 /g and the macropores fraction rises from 3.58% to 5.03% at 20% WG incorporation.
(3) After exposure to high temperatures, a threshold is observed at 20% WG substitution. Samples with WG content below this threshold exhibit increased compressive strength with rising temperature, whereas those with higher WG contents experience

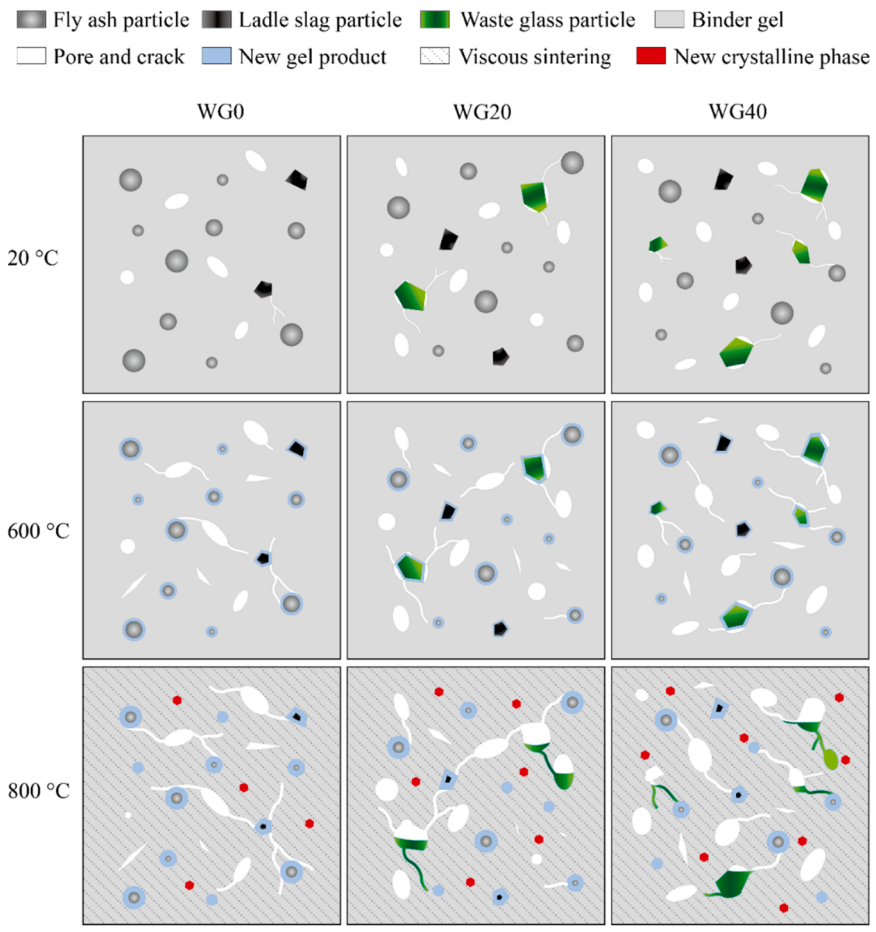

Fig. 21. Schematic diagram of the physical and chemical evolution of the blends at high temperatures.

strength reduction at 800 °C. Notably, the incorporation of 20% WG results in the greatest strength enhancement, with compressive strength value of 31.14 MPa, which is 2.57 times that of the sample at 20 °C.

(4) The WG reactivity is progressively activated as temperature increases, facilitating the release of more Ca into the system, and the gel products of samples containing WG shift towards both Ca-enriched and Al-enriched structures. With the temperature rising from 20 °C to 600 °C, the addition of WG causes greater gel dehydration, resulting in pore structure coarsening while simultaneously promoting the formation of denser gel clusters, which enhance micromechanical strength and improve overall compressive strength.

(5) At 800 °C, the 20% WG plays a physical reinforcement and chemical strengthening role. With a pore system similar to that of the reference group, WG20 develops more thermally stable crystalline phases, especially the wollastonite and nepheline phases, due to the recrystallization from gel products and residual WG, thereby enhancing compressive strength.

From the perspective of engineering applications, although the ambient compressive strength of the developed binder is relatively moderate, the material shows potential for various fire-resistant applications, such as fireproof panels, protective layers or linings, and refractory repair materials, where thermal stability and post-fire integrity are critical. The significant increase in residual strength further indicates the improved effect of WG upon heating, which can enhance fire-resistant capacity and higher safety margins. Nevertheless, further optimization remains necessary to improve the ambient strength and mitigate the risk of dimensional instability and pore coarsening when excessive WG is incorporated, so as to achieve a better balance between workability, ambient-temperature performance and high-temperature resistance.

CRediT authorship contribution statement

Xuan Ling: Investigation. **Yan Luo:** Investigation. **Yanjie Tang:** Investigation. **H.J.H. Brouwers:** Supervision, Funding acquisition. **Yanshuo Liu:** Investigation. **Qingliang Yu:** Writing – review & editing, Supervision, Project administration, Funding acquisition, Conceptualization. **Jiale Yuan:** Writing – original draft, Validation, Methodology, Investigation, Formal analysis, Data curation.

Declaration of Competing Interest

The authors declare that they have no known competing financial interests or personal relationships that could have appeared to influence the work reported in this paper.

Acknowledgments

This research is supported by China Scholarship Council (No. 202306950009) and the Department of the Built Environment at Eindhoven University of Technology.

Data Availability

Data will be made available on request.

References

[1] W. Tu, M. Zhang, Behaviour of alkali-activated concrete at elevated temperatures: A critical review, Cem. Concr. Compos 138 (2023) 104961, https://doi.org/10.1016/j.cemconcomp.2023.104961.

[2] J. Krejsová, R. Černý, Physical and chemical processes in alkali-activated aluminosilicates at high temperatures and their effect on functional properties: A critical review, Cem. Concr. Compos 162 (2025) 106143, https://doi.org/10.1016/j.cemconcomp.2025.106143.

[3] T. Manzoor, J.A. Bhat, A.H. Shah, Performance of geopolymer concrete at elevated temperature – A critical review, Constr. Build. Mater. 420 (2024) 135578, https://doi.org/10.1016/j.conbuildmat.2024.135578.

[4] I. Ismail, S.A. Bernal, J.L. Provis, R. San Nicolas, S. Hamdan, J.S.J. Van Deventer, Modification of phase evolution in alkali-activated blast furnace slag by the incorporation of fly ash, Cem. Concr. Compos 45 (2014) 125–135, https://doi.org/10.1016/j.cemconcomp.2013.09.006.

[5] W.G. Valencia Saavedra, R. Mejía De Gutiérrez, Performance of geopolymer concrete composed of fly ash after exposure to elevated temperatures, Constr. Build. Mater. 154 (2017) 229–235, https://doi.org/10.1016/j.conbuildmat.2017.07.208.

[6] S.J. Chithambaram, S. Kumar, M.M. Prasad, Thermo-mechanical characteristics of geopolymer mortar, Constr. Build. Mater. 213 (2019) 100–108, https://doi.org/10.1016/j.conbuildmat.2019.04.051.

[7] Y. Luo, H.J.H. Brouwers, Q. Yu, Understanding the gel compatibility and thermal behavior of alkali activated Class F fly ash/ladle slag: The underlying role of Ca availability, Cem. Concr. Res. 170 (2023) 107198, https://doi.org/10.1016/j.cemconres.2023.107198.

[8] S.M. Park, J.G. Jang, N.K. Lee, H.K. Lee, Physicochemical properties of binder gel in alkali-activated fly ash/slag exposed to high temperatures, Cem. Concr. Res. 89 (2016) 72–79, https://doi.org/10.1016/j.cemconres.2016.08.004.

[9] W. Tu, G. Fang, B. Dong, Y. Hu, M. Zhang, Behaviour of alkali-activated fly ash-slag paste at elevated temperatures: An experimental study, Cem. Concr. Compos 147 (2024) 105438, https://doi.org/10.1016/j.cemconcomp.2024.105438.

[10] Z. Zhang, J.L. Provis, A. Reid, H. Wang, Mechanical, thermal insulation, thermal resistance and acoustic absorption properties of geopolymer foam concrete, Cem. Concr. Compos 62 (2015) 97–105, https://doi.org/10.1016/j.cemconcomp.2015.03.013.

[11] M.U. Yılmazoğlu, H.O. Kara, A. Benli, A.R. Demirkıran, O.Y. Bayraktar, G. Kaplan, Sustainable alkali-activated foam concrete with pumice aggregate: effects of clinoptilolite zeolite and fly ash on strength, durability, and thermal performance, Constr. Build. Mater. 464 (2025) 140160, https://doi.org/10.1016/j.conbuildmat.2025.140160.

[12] Z. Deng, Z. Yang, J. Bian, J. Lin, Z. Long, G. Hong, Z. Yang, Y. Ye, Advantages and disadvantages of PVA-fibre-reinforced slag- and fly ash-blended geopolymer composites: Engineering properties and microstructure, Constr. Build. Mater. 349 (2022) 128690, https://doi.org/10.1016/j.conbuildmat.2022.128690.

[13] M. Yu, T. Wang, Y. Chi, D. Li, L. Li, F. Shi, Residual mechanical properties of GGBS-FA-SF blended geopolymer concrete after exposed to elevated temperatures, Constr. Build. Mater. 411 (2024) 134378, https://doi.org/10.1016/j.conbuildmat.2023.134378.

[14] C.L. Chan, M. Zhang, Behaviour of strain hardening geopolymer composites at elevated temperatures, Cem. Concr. Compos 132 (2022) 104634, https://doi.org/10.1016/j.cemconcomp.2022.104634.

[15] Y. Luo, K.M. Klima, H.J.H. Brouwers, Q. Yu, Effects of ladle slag on Class F fly ash geopolymer: Reaction mechanism and high temperature behavior, Cem. Concr. Compos 129 (2022) 104468, https://doi.org/10.1016/j.cemconcomp.2022.104468.

[16] A. Natali Murri, W.D.A. Rickard, M.C. Bignozzi, A. Van Riessen, High temperature behaviour of ambient cured alkali-activated materials based on ladle slag, Cem. Concr. Res. 43 (2013) 51–61, https://doi.org/10.1016/j.cemconres.2012.09.011.

[17] J. Lu, C. Poon, Use of waste glass in alkali activated cement mortar, Constr. Build. Mater. 160 (2018) 399–407, https://doi.org/10.1016/j.conbuildmat.2017.11.080.

[18] A.N. Derinpinar, M.B. Karakoç, A. Özcan, Performance of glass powder substituted slag based geopolymer concretes under high temperature, Constr. Build. Mater. 331 (2022) 127318, https://doi.org/10.1016/j.conbuildmat.2022.127318.

[19] X. Jiang, R. Xiao, Y. Ma, M. Zhang, Y. Bai, B. Huang, Influence of waste glass powder on the physico-mechanical properties and microstructures of fly ash-based geopolymer paste after exposure to high temperatures, Constr. Build. Mater. 262 (2020) 120579, https://doi.org/10.1016/j.conbuildmat.2020.120579.

[20] Y. Huang, Z. Chen, Y. Liu, J. Lu, Z. Bian, M. Yio, C. Cheeseman, F. Wang, C. Sun Poon, Recycling of waste glass and incinerated sewage sludge ash in glass-ceramics, Waste Manag 174 (2024) 229–239, https://doi.org/10.1016/j.wasman.2023.12.007.

[21] S. Yoon, J. Lee, J. Lee, Y. Yun, W. Yoon, Characterization of wollastonite glass-ceramics made from waste glass and coal fly ash, J. Mater. Sci. Technol. 29 (2013) 149–153, https://doi.org/10.1016/j.jmst.2012.12.002.

[22] L. Zeng, H. Sun, T. Peng, T. Hui, Effect of glass content on sintering kinetics, microstructure and mechanical properties of glass-ceramics from coal fly ash and waste glass, Mater. Chem. Phys. 260 (2021) 124120, https://doi.org/10.1016/j.matchemphys.2020.124120.

[23] K. Lin, T. Lee, C. Hwang, Effects of sintering temperature on the characteristics of solar panel waste glass in the production of ceramic tiles, J. Mater. Cycles Waste Manag 17 (2015) 194–200, https://doi.org/10.1007/s10163-014-0240-3.

[24] K. Lin, T. Chu, C. Cheng, C. Lee, T. Chang, K.-S. Wang, Recycling solar panel waste glass sintered as glass-ceramics, Environ. Prog. Sustain. Energy 31 (2012) 612–618, https://doi.org/10.1002/ep.10587.

[25] S.Y. Yao, H.X. Cao, P. Wang, W.W. Zhang, W.L. Huo, W. Xu, Phase transformation and microstructure of wollastonite glass–ceramics in Na_2O–CaO–SiO_2 system under different heat treatment conditions, Mater. Res. Innov. 18 (2014) S4-657–S4-660, https://doi.org/10.1179/1432891714Z.000000000763.

[26] Y. Luo, S.H. Li, K.M. Klima, H.J.H. Brouwers, Q. Yu, Degradation mechanism of hybrid fly ash/slag based geopolymers exposed to elevated temperatures, Cem. Concr. Res. 151 (2022) 106649, https://doi.org/10.1016/j.cemconres.2021.106649.

[27] M.J. De Hita, M. Criado, Influence of superplasticizers on the workability and mechanical development of binary and ternary blended cement and alkali-activated cement, Constr. Build. Mater. 366 (2023) 130272, https://doi.org/10.1016/j.conbuildmat.2022.130272.

[28] S. Li, J. Zhang, Z. Li, Y. Gao, C. Liu, Feasibility study of red mud-blast furnace slag based geopolymeric grouting material: Effect of superplasticizers, Constr. Build. Mater. 267 (2021) 120910, https://doi.org/10.1016/j.conbuildmat.2020.120910.

[29] M.H. Samarakoon, P.G. Ranjith, V.R.S. De Silva, Effect of soda-lime glass powder on alkali-activated binders: Rheology, strength and microstructure characterization, Constr. Build. Mater. 241 (2020) 118013, https://doi.org/10.1016/j.conbuildmat.2020.118013.

[30] J.X. Lu, Z.H. Duan, C.S. Poon, Combined use of waste glass powder and cullet in architectural mortar, Cem. Concr. Compos 82 (2017) 34–44, https://doi.org/10.1016/j.cemconcomp.2017.05.011.

[31] I.C. Carvalho, A.R. Chaves, C.L. Araújo, H.N. Costa, A.E.B. Cabral, Mechanical, rheological, and microstructural study of ternary alkali-activated pastes using bof slag, metakaolin, and glass powder as precursors, J. Mater. Civ. Eng. 36 (2024) 04024121, https://doi.org/10.1061/JMCEE7.MTENG-17132.

[32] J. Wen, Y. Wan, Y. Yang, Sustainable synthesis of hydrophobic waste glass powder for enhanced water and frost resistance in mortar, Constr. Build. Mater. 487 (2025) 142097, https://doi.org/10.1016/j.conbuildmat.2025.142097.

[33] Y. Zhang, R. Xiao, X. Jiang, W. Li, X. Zhu, B. Huang, Effect of particle size and curing temperature on mechanical and microstructural properties of waste glass-slag-based and waste glass-fly ash-based geopolymers, J. Clean. Prod. 273 (2020) 122970, https://doi.org/10.1016/j.jclepro.2020.122970.

[34] O.G. Rivera, W.R. Long, C.A. Weiss Jr., R.D. Moser, B.A. Williams, K. Torres-Cancel, E.R. Gore, P.G. Allison, Effect of elevated temperature on alkali-activated geopolymeric binders compared to portland cement-based binders, Cem. Concr. Res. 90 (2016) 43–51, https://doi.org/10.1016/j.cemconres.2016.09.013.

[35] J. Ren, L. Zhang, B. Walkley, J.R. Black, R.S. Nicolas, Degradation resistance of different cementitious materials to phosphoric acid attack at early stage, Cem. Concr. Res. 151 (2022) 106606, https://doi.org/10.1016/j.cemconres.2021.106606.

[36] Y.S. Ng, Y.M. Liew, C.Y. Heah, M.M.A.B. Abdullah, C. Rojviriya, M.S. Khalid, S. W. Ong, W.E. Ooi, Y.J. Hang, Interaction of silica fume on flexural properties of 10 mm-thickness geopolymers based on fly ash and ladle furnace slag under the thermal conditions, J. Build. Eng. 69 (2023) 106331, https://doi.org/10.1016/j.jobe.2023.106331.

[37] M.R. Ahmad, L.P. Qian, Y. Fang, A. Wang, J.G. Dai, A multiscale study on gel composition of hybrid alkali-activated materials partially utilizing air pollution control residue as an activator, Cem. Concr. Compos 136 (2023) 104856, https://doi.org/10.1016/j.cemconcomp.2022.104856.

[38] G. Fang, M. Zhang, Multiscale micromechanical analysis of alkali-activated fly ash-slag paste, Cem. Concr. Res. 135 (2020) 106141, https://doi.org/10.1016/j.cemconres.2020.106141.

[39] M. Torres-Carrasco, F. Puertas, Waste glass as a precursor in alkaline activation: Chemical process and hydration products, Constr. Build. Mater. 139 (2017) 342–354, https://doi.org/10.1016/j.conbuildmat.2017.02.071.

[40] W. Tu, G. Fang, B. Dong, M. Zhang, Multiscale study of microstructural evolution in alkali-activated fly ash-slag paste at elevated temperatures, Cem. Concr. Compos 143 (2023) 105258, https://doi.org/10.1016/j.cemconcomp.2023.105258.

[41] X. Ling, W. Chen, K. Schollbach, H.J.H. Brouwers, Low permeability sealing materials based on sewage, digestate and incineration industrial by-products in the final landfill cover system, Constr. Build. Mater. 412 (2024) 134889, https://doi.org/10.1016/j.conbuildmat.2024.134889.

[42] P. Praneedpolkrang, N. Chaiwasee, P. Koedmontree, A. Suthiwong, H. Kaur, C. Jaturapitakkul, W. Tangchirapat, Effects of elevated temperature on mechanical properties and microstructures of alkali-activated mortar made from low calcium fly ash-calcium carbide residue mixture, Case Stud. Constr. Mater. 21 (2024) e03520, https://doi.org/10.1016/j.cscm.2024.e03520.

[43] I. Garcia-Lodeiro, A. Palomo, A. Fernández-Jiménez, D.E. Macphee, Compatibility studies between N-A-S-H and C-A-S-H gels. Study in the ternary diagram Na_2O–CaO–Al_2O_3–SiO_2–H_2O, Cem. Concr. Res. 41 (2011) 923–931, https://doi.org/10.1016/j.cemconres.2011.05.006.

[44] P. Yu, R.J. Kirkpatrick, B. Poe, P.F. McMillan, X. Cong, Structure of Calcium Silicate Hydrate (C-S-H): Near-, Mid-, and Far-Infrared Spectroscopy, J. Am. Ceram. Soc. 82 (1999) 742–748, https://doi.org/10.1111/j.1151-2916.1999.tb01826.x.

[45] I. Garcia-Lodeiro, A. Fernández-Jiménez, M.T. Blanco, A. Palomo, FTIR study of the sol–gel synthesis of cementitious gels: C–S–H and N–A–S–H, J. Sol. -Gel Sci. Technol. 45 (2008) 63–72, https://doi.org/10.1007/s10971-007-1643-6.

[46] K. Sun, H.A. Ali, D. Xuan, C.S. Poon, Sulfuric acid resistance behaviour of alkali-activated slag and waste glass powder blended precursors, Cem. Concr. Compos 145 (2024) 105319, https://doi.org/10.1016/j.cemconcomp.2023.105319.

[47] T. Liu, C. Gong, L. Duan, B. Qu, Effects of sodium citrate on compressive strength and microstructure of NaOH-activated fly ash/slag cement exposed to high temperature, Constr. Build. Mater. 363 (2023) 129852, https://doi.org/10.1016/j.conbuildmat.2022.129852.

[48] S. Palakurthy, K. V.G.R, R.K. Samudrala, P. A.A, vitro bioactivity and degradation behaviour of β-wollastonite derived from natural waste, Mater. Sci. Eng. C. 98 (2019) 109–117, https://doi.org/10.1016/j.msec.2018.12.101.
[49] X. Jiang, Y. Zhang, R. Xiao, P. Polaczyk, M. Zhang, W. Hu, Y. Bai, B. Huang, A comparative study on geopolymers synthesized by different classes of fly ash after exposure to elevated temperatures, J. Clean. Prod. 270 (2020) 122500, https://doi.org/10.1016/j.jclepro.2020.122500.
[50] Z. Pan, Z. Tao, Y.F. Cao, R. Wuhrer, T. Murphy, Compressive strength and microstructure of alkali-activated fly ash/slag binders at high temperature, Cem. Concr. Compos 86 (2018) 9–18, https://doi.org/10.1016/j.cemconcomp.2017.09.011.
[51] D.L.Y. Kong, J.G. Sanjayan, K. Sagoe-Crentsil, Comparative performance of geopolymers made with metakaolin and fly ash after exposure to elevated temperatures, Cem. Concr. Res. 37 (2007) 1583–1589, https://doi.org/10.1016/j.cemconres.2007.08.021.
[52] P. Rovnaník, P. Bayer, P. Rovnaníková, Characterization of alkali activated slag paste after exposure to high temperatures, Constr. Build. Mater. 47 (2013) 1479–1487, https://doi.org/10.1016/j.conbuildmat.2013.06.070.
[53] B. Walkley, R.S. Nicolas, M. Sani, G.J. Rees, J.V. Hanna, Phase evolution of C-(N)-A-S-H/N-A-S-H gel blends investigated via alkali-activation of synthetic calcium aluminosilicate precursors, Cem. Concr. Res. (2016), https://doi.org/10.1016/j.cemconres.2016.08.010.
[54] W. Tu, G. Fang, B. Dong, M. Zhang, Micromechanical analysis of alkali-activated fly ash-slag paste subjected to elevated temperatures, Cem. Concr. Compos 153 (2024) 105735, https://doi.org/10.1016/j.cemconcomp.2024.105735.
[55] K.M. Klima, K. Schollbach, H.J.H. Brouwers, Q. Yu, Thermal and fire resistance of Class F fly ash based geopolymers – A review, Constr. Build. Mater. 323 (2022) 126529, https://doi.org/10.1016/j.conbuildmat.2022.126529.
[56] Z. Pan, J.G. Sanjayan, Factors influencing softening temperature and hot-strength of geopolymers, Cem. Concr. Compos 34 (2012) 261–264, https://doi.org/10.1016/j.cemconcomp.2011.09.019.
[57] P. Duxson, G.C. Lukey, J.S.J. Van Deventer, Thermal evolution of metakaolin geopolymers: Part 1 – Physical evolution, J. Non-Cryst. Solids 352 (2006) 5541–5555, https://doi.org/10.1016/j.jnoncrysol.2006.09.019.
[58] M. Wang, J. Cheng, Viscosity and thermal expansion of rare earth containing soda-lime-silicate glass, J. Alloy. Compd. 504 (2010) 273–276, https://doi.org/10.1016/j.jallcom.2010.05.111.
[59] W.M. Zheng, H.J. Sun, T.J. Peng, L. Zeng, Novel preparation of foamed glass-ceramics from asbestos tailings and waste glass by self-expansion in high temperature, J. Non-Cryst. Solids 529 (2020) 119767, https://doi.org/10.1016/j.jnoncrysol.2019.119767.